Inverse methods for quantifying time-varying subglacial perturbations from altimetry

Aaron G. Stubblefield[1]

[1]Lamont-Doherty Earth Observatory, Columbia University

Key Points:

- Altimetry-based inverse methods for quantifying time-varying subglacial perturbations are developed
- Incorporating surface velocity data facilitates reconstruction of multiple parameter fields or refinement of altimetry-based inversions
- Potential applications of the methods include quantification of subglacial lake activity and slippery or sticky spots beneath ice sheets

Corresponding author: Aaron Stubblefield, `aaron@ldeo.columbia.edu`

Abstract

Glacier surface elevation responds to a variety of localized processes occurring beneath the ice. Subglacial-lake volume change in particular is inherently time-dependent, producing time-varying perturbations in ice-surface elevation. Here, we introduce inverse methods for quantifying time-varying subglacial perturbations from altimetry data and, when available, horizontal surface velocity data. The forward model is based on a small-perturbation approximation of the Stokes equations that is solved efficiently with Fourier transform methods. The inverse methods are derived from variational least-squares optimization problems and the associated normal equations are solved with the conjugate gradient method. We conduct synthetic tests for reconstructing time-varying basal vertical velocity and drag perturbations that are motivated by subglacial-lake activity and slippery spots beneath Antarctic ice streams. We show that incorporation of horizontal surface velocity data as additional constraints can refine altimetry-based inversions or facilitate reconstruction of multiple fields, depending on whether the data are spatially discrete or continuous. We further validate the method by showing that it can reconstruct basal perturbations from synthetic elevation data that are produced by a nonlinear subglacial lake model. With the advent of high spatial and temporal resolution altimetry data from NASA's ICESat-2 mission, these inverse methods will facilitate further assessment of the relation between ice-sheet flow and subglacial processes.

Plain Language Summary

The topography of glaciers and ice sheets changes over time due to a variety of processes that operate over a range of spatial and temporal scales. While large-scale ice flow is influenced by climate change on decadal to centennial timescales, uncertainty remains in how these changes relate to small-scale or "local" processes that often occur on shorter timescales. Local changes in glacier topography are often associated with phenomena occurring beneath the ice such as the presence of subglacial lakes, flow over anomalous bedrock topography, or melting of the ice. Here, we develop computational methods that use elevation data to quantify a variety of phenomena occurring beneath glaciers and ice sheets. With the advent of high-resolution elevation data from NASA's ICESat-2 satellite altimetry mission, these methods will facilitate assessment of the relation between a variety of dynamic subglacial processes and the flow of Earth's ice sheets.

1 Introduction

Ice-sheet surface elevation responds to a variety of time-varying subglacial phenomena, including subglacial-lake volume change, basal-drag variations, and melting of the basal ice. Subglacial lakes in particular have received much attention due to the localized perturbations they produce in ice-sheet surface elevation during volume-change events (Gray et al., 2005; Fricker et al., 2007; Wingham et al., 2006). The ICESat (NASA) and CryoSat-2 (ESA) satellite altimetry missions facilitated the detection of hundreds of subglacial lakes beneath the Antarctic Ice Sheet (Fricker et al., 2016; Smith et al., 2009; Wright & Siegert, 2012), raising investigations into their possible relation to fast ice flow (Scambos et al., 2011; Siegfried et al., 2016; Stearns et al., 2008) and ability to host microbial ecosystems (e.g., Achberger et al., 2016; Christner et al., 2014). Few subglacial lakes have been discovered beneath the Greenland Ice Sheet based on ice-surface changes, suggesting that there may be fundamental differences in subglacial conditions there relative to the Antarctic Ice Sheet (Bowling et al., 2019; Livingstone et al., 2019).

High-resolution satellite altimetry data from NASA's ICESat-2 mission presents an invaluable opportunity to continue investigating dynamic conditions beneath ice sheets (Abdalati et al., 2010; Markus et al., 2017; Neckel et al., 2021; Siegfried & Fricker, 2021). While ice-surface elevation changes provide clues about subglacial hydrological activity, modelling has shown that accurately estimating subglacial-lake volume change, areal extent, and highstand or lowstand timing from altimetry alone is often infeasible due to the effects of viscous ice flow (Stubblefield, Creyts, et al., 2021). Inverse methods that quantify subglacial-lake activity from altimetry while accounting for ice-flow effects have not yet been developed.

Subglacial lakes or anomalous bed topography can be associated with basal drag anomalies that produce adjacent areas of thickening and thinning (Bell et al., 2007; Fricker et al., 2010; O. V. Sergienko et al., 2007; O. V. Sergienko & Hulbe, 2011; Shapero et al., 2016; Winberry et al., 2014). These anomalies are often called 'sticky' or 'slippery' spots, depending on whether they are a local enhancement or reduction in drag, respectively. Many previous basal drag coefficient inversions rely on velocity data without incorporating altimetry data as constraints in the optimization problem (Arthern & Gudmundsson, 2010; D. N. Goldberg & Sergienko, 2011; Joughin et al., 2004; MacAyeal, 1993; MacAyeal et al., 1995; Morlighem et al., 2010, 2013; Petra et al., 2012; Ranganathan et al., 2021; Vieli & Payne, 2003). However, satellite altimetry data is increasingly being used in basal drag inversions that rely on depth-integrated approximations of the Stokes equations (Arthern et al., 2015; D. Goldberg & Heimbach, 2013; D. Goldberg et al., 2015; Larour et al., 2014; Mosbeux et al., 2016).

Inversion of time-varying altimetry or velocity data benefits from dimensionality reduction to alleviate the computational cost associated with repeatedly solving the forward problem. Dimensionality reduction is often achieved through utilization of depth-integrated ice-flow models (Greve & Blatter, 2009, ch. 5). Applying perturbation methods to the Stokes equations is an alternative way to achieve computational efficiency when the full stresses in the ice must be resolved (e.g., Balise & Raymond, 1985; Bassis & Ma, 2015; Budd, 1970; Gudmundsson et al., 1998; Gudmundsson, 2003; Hutter et al., 1981; Reeh, 1987; O. Sergienko, 2012; Stubblefield, Creyts, et al., 2021). The primary limitations of (first-order) perturbation methods are that the resulting forward models are inherently linear, posed on geometrically simple domains, and cannot deviate significantly from the specified background state. Previous inversions relying on perturbation methods have not included time-varying data (Gudmundsson & Raymond, 2008; Thorsteinsson et al., 2003). Likewise, a general framework for inversion of time-varying elevation or velocity data with perturbation-based models has not been developed.

Here, we derive and test altimetry-based inverse methods for quantifying basal vertical velocity or drag coefficient perturbations that arise from subglacial lakes or anomalous bed topography. First, we outline the forward model for the perturbation in ice-surface elevation that is produced by basal forcing (Section 2). We then derive methods for altimetry-based inversions (Section 3.1) and joint inversions that incorporate horizontal surface velocity data as additional constraints (Section 3.2). To illustrate the methods and their applicability, we conduct synthetic tests that are motivated by subglacial lake activity and slippery spots by inverting synthetic data produced with the small-perturbation model (Section 4.1) and a nonlinear subglacial lake model (Section 4.2). We conclude by discussing applications, limitations, and extensions of the methods (Section 5).

2 Forward Model

Here, we outline the forward model for the perturbation in ice-surface elevation given different types of basal perturbations as input (Figure 1). The model is based on a small-perturbation approximation of the Stokes equations that closely follows previous work (e.g., Balise & Raymond, 1985; Gudmundsson et al., 1998; Gudmundsson, 2003). We provide a detailed derivation of the model in the Supporting Information (Text S1). In this section, we describe the background states (Section 2.1), primary mathematical operations (Section 2.2), model equations (Section 2.3), a scaling of the problem (Section 2.5), and the ice-surface elevation anomaly solutions (Section 2.6).

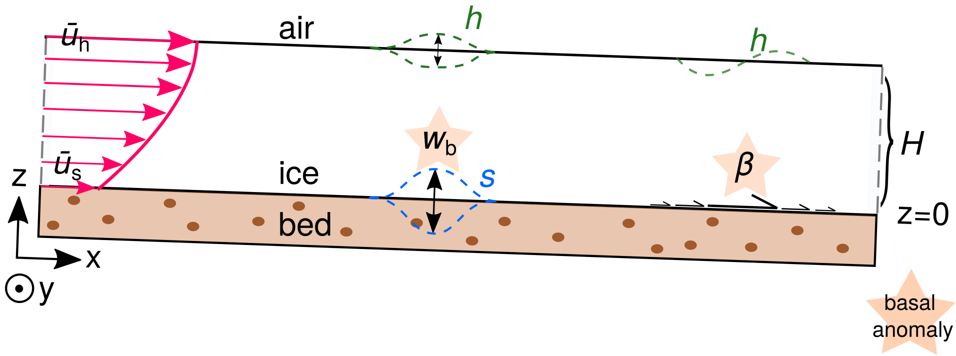

Figure 1. Sketch of model setup depicting the basal anomalies (w_b, β), ice-surface elevation anomaly (h), basal-surface elevation anomaly (s), and background ice thickness (H). Background flow profiles are shown in red, with $\bar{u}_h$ and $\bar{u}_s$ denoting the surface and basal background flow speeds, respectively. There is no background flow in the direction of the y axis, which is oriented perpendicular to the page. The coordinate system is rotated to coincide with the background bed slope (α).

2.1 Background States and Perturbations

We assume that all fields are small, localized perturbations from a background state that satisfies the incompressible Stokes equations with Newtonian viscosity, η (Text S1). The spatial domain is a strip of finite vertical thickness, H, and infinite horizontal extent in three-dimensional (x, y, z) space. The coordinate system is rotated to coincide with the background bed slope $\alpha \geq 0$ (Figure 1). At the basal surface, the vertical velocity is prescribed along with a linear sliding law that relates the horizontal velocity and shear stress. We assume a stress-free condition at the upper surface. Finally, the Stokes problem is coupled to kinematic equations that describe the evolution of the upper and basal surfaces (Text S1).

We set the background ice-surface elevation to be $\bar{h} = H$, the background basal surface elevation to be $\bar{s} = 0$, the background accumulation rate to be $\bar{a} = 0$, the background basal melting rate to be $\bar{m} = 0$, the background horizontal velocity in the y-direction to be $\bar{v} = 0$, and the background vertical velocity to be $\bar{w} = 0$. We let $\bar{u}_s$ denote the background basal sliding velocity and $\bar{u}_h$ the background horizontal surface velocity in the x direction, respectively (Figure 1). We consider the parabolic velocity solutions

$$\bar{u} = \bar{u}_s + \frac{\rho g \sin(\alpha)}{2\eta}(H^2 - (H-z)^2), \quad \bar{p} = \rho g \cos(\alpha)(H - z), \quad \bar{\beta}\bar{u}_s = \rho g \sin(\alpha) H, \qquad (1)$$

where $\bar{u}$ is the background horizontal velocity in the x-direction, $\bar{p}$ is the background ice pressure, $\bar{\beta}$ is the background basal drag coefficient, g is gravitational acceleration, and ρ is the ice density. In the limit $\alpha \to 0$, equation (1) reduces to a uniform flow in the x-direction with either free slip ($\bar{\beta} = 0$) or no sliding ($\bar{u}_s = 0$). We define the model parameters related to these background states in Table 1.

We consider perturbations in the basal vertical velocity, w_b, and basal drag coefficient, β, relative to the above background state (eq. 1). For example, the basal vertical velocity anomaly w_b may be produced from either bed topography or subglacial lake activity. Likewise, the basal drag perturbation may be related to a "slippery spot" ($\beta < 0$) associated with the presence of subglacial water or "sticky spot" ($\beta > 0$) associated with bed roughness. These basal perturbations cause perturbations in the ice-surface elevation, h, and the basal surface elevation, s. We also consider perturbations in basal melting rate, m, and accumulation (or ablation) rate, a, although these are not included in the inversion examples for simplicity. We illustrate the background states and perturbations in Figure 1.

2.2 Main Operations

The solution method relies on the map-plane Fourier transform, which for a function $f(x, y)$ is given by

$$\widehat{f}(k_x, k_y) = \int_{-\infty}^{+\infty} \int_{-\infty}^{+\infty} f(x, y) e^{-i(k_x x + k_y y)} \, \mathrm{d}x \, \mathrm{d}y, \tag{2}$$

where k_x and k_y are wavenumbers corresponding to the x and y directions, respectively. We denote the length of the wavevector by

$$k = \sqrt{k_x^2 + k_y^2}. \tag{3}$$

A function f may be recovered with the inverse Fourier transform via

$$f(x, y) = \frac{1}{4\pi^2} \int_{-\infty}^{+\infty} \int_{-\infty}^{+\infty} \widehat{f}(k_x, k_y) e^{i(k_x x + k_y y)} \, \mathrm{d}k_x \, \mathrm{d}k_y. \tag{4}$$

We will also rely on the convolution of two functions $f_1(t)$ and $f_2(t)$ over time t, which is given by

$$f_1 * f_2 = \int_0^t f_1(\tilde{t}) f_2(t - \tilde{t}) \, \mathrm{d}\tilde{t}, \tag{5}$$

provided that these functions vanish for $t < 0$.

2.3 Model Equations

Under the assumption of small, localized perturbations, the ice-surface elevation anomaly h evolves in frequency space via

$$\frac{\partial \widehat{h}}{\partial t} + [ik_x \bar{u}_h + \mathsf{R}_g] \, \widehat{h} = \widehat{a} + \mathsf{T}_w \widehat{w}_b + ik_x \mathsf{T}_\beta (\bar{u}_s \widehat{\beta} - \bar{\tau} \widehat{s}) \tag{6}$$

in response to anomalies in the basal vertical velocity w_b, basal drag coefficient β, surface accumulation (or ablation) a, and basal surface elevation s (Text S1). Likewise, the basal surface s evolves according to

$$\frac{\partial \widehat{s}}{\partial t} + ik_x \bar{u}_s \widehat{s} = \widehat{w}_b + \widehat{m}, \tag{7}$$

where m is the basal melting rate. The terms $ik_x \bar{u}_h \widehat{h}$ and $ik_x \bar{u}_s \widehat{s}$ in (6) and (7), respectively, represent surface advection from the background flow.

The function R_g in equation (6) describes relaxation of the ice-sheet surface, and is given by

$$\mathsf{R}_g = \left(\frac{\rho g \cos(\alpha)}{2\eta k} \right) \frac{(1+\gamma) e^{4k'} - (2 + 4\gamma k' - 4c_\alpha k'(1 + \gamma k')) e^{2k'} + 1 - \gamma}{(1+\gamma) e^{4k'} + (2\gamma + 4k' + 4\gamma k'^2) e^{2k'} - 1 + \gamma}, \tag{8}$$

where we have defined the nondimensional quantities

$$k' = kH, \quad c_\alpha = (ik_x/k) \tan(\alpha), \quad \gamma = \tilde{\beta}/k', \quad \tilde{\beta} = \frac{\bar{\beta} H}{2\eta}. \tag{9}$$

In the limit of a horizontal bed ($\alpha \to 0$) and infinite ice thickness ($k' \to \infty$), R_g (eq. 8) reduces to the classical topographic relaxation frequency, $\rho g/(2\eta k)$ (Turcotte & Schubert, 2002). This infinite-thickness relaxation frequency is an upper bound on R_g.

The function T_w in equation (6) describes transfer of the basal vertical velocity anomaly w_b to its surface expression, and is given by

$$\mathsf{T}_w = \frac{2(1+\gamma)(k'+1)e^{3k'} + 2(1-\gamma)(k'-1)e^{k'}}{(1+\gamma)e^{4k'} + (2\gamma + 4k' + 4\gamma k'^2)e^{2k'} - 1 + \gamma}. \tag{10}$$

The velocity transfer function produces a diminished surface expression of the basal anomaly because $\mathsf{T}_w \leq 1$ for all $k' \geq 0$ (Figure 2). In the limit of no basal sliding ($\gamma \to \infty$), equation (10) reduces to the vertical velocity transfer function derived by Balise and Raymond (1985, eq. 21b therein).

Finally, the function T_β in equation (6) describes the influence of basal drag anomalies on elevation change, and is given by

$$\mathsf{T}_\beta = \left(\frac{k'}{\eta k^2}\right) \frac{e^{3k'} + e^{k'}}{(1+\gamma)e^{4k'} + (2\gamma + 4k' + 4\gamma k'^2)e^{2k'} - 1 + \gamma}. \tag{11}$$

While basal drag anomalies can result directly from the anomaly β, equation (6) shows that they can also arise indirectly from basal surface perturbations s. Drag perturbations result from basal surface perturbations when there are vertical gradients in the background sliding speed or shear stress, which are encoded in the stress-gradient parameter

$$\bar{\tau} = \bar{\beta}\bar{u}_z - \eta \bar{u}_{zz}|_{z=0}. \tag{12}$$

The background basal stress gradient $\bar{\tau}$ (eq. 12) is computed from the background state parameters (Table 1).

2.4 Scaling

Now, we introduce scalings for the forward model equations (6) and (7). We let h_0 be a measure of the elevation anomaly magnitude and t_0 a measure of the observational timescale (Table 1). We scale the variables according to

$$\begin{aligned} &h = h_0 h', \quad s = h_0 s', \quad w_b = \frac{h_0}{t_0} w_b', \quad \beta = \frac{2\eta}{H}\beta', \qquad m = \frac{h_0}{t_0} m', \qquad a = \frac{h_0}{t_0} a' \\ &x = Hx', \quad y = Hy', \quad t = t_0 t', \quad k = H^{-1}k', \quad k_x = H^{-1}k_x', \quad k_y = H^{-1}k_y', \end{aligned} \tag{13}$$

where primes denote dimensionless quantities. We provide representative values for these scales in Table 1.

In equation (6), we scale the relaxation function R_g (eq. 8) according to

$$\mathsf{R}_g = t_r^{-1}\mathsf{R}_g', \quad \mathsf{R}_g' = \frac{1}{k'} \frac{(1+\gamma)e^{4k'} - (2 + 4\gamma k' - 4c_\alpha k'(1+\gamma k'))e^{2k'} + 1 - \gamma}{(1+\gamma)e^{4k'} + (2\gamma + 4k' + 4\gamma k'^2)e^{2k'} - 1 + \gamma} \tag{14}$$

where

$$t_r = \frac{2\eta}{\rho_i g \cos(\alpha) H} \tag{15}$$

is the characteristic timescale for viscous relaxation of surface topography perturbations with H^{-1} wavenumber (c.f. Turcotte & Schubert, 2002). Similarly, we define the scaled basal-drag transfer function to be

$$\mathsf{T}_\beta'(k') = \frac{2}{k'} \frac{e^{3k'} + e^{k'}}{(1+\gamma)e^{4k'} + (2\gamma + 4k' + 4\gamma k'^2)e^{2k'} - 1 + \gamma}. \tag{16}$$

The velocity transfer function T_w (eq. 10) is already nondimensional, depending only on k'. We show the scaled relaxation and transfer functions over a range of wavenumbers in Figure 2.

Omitting primes on the variables, we scale the elevation anomaly equation (6) to obtain

$$\frac{\partial \widehat{h}}{\partial t} + [ik_x\tilde{u}_h + \lambda \mathsf{R}_g]\,\widehat{h} = \widehat{a} + \mathsf{T}_w\widehat{w}_b + ik_x\mathsf{T}_\beta(\nu\widehat{\beta} - \tilde{\tau}\widehat{s}), \tag{17}$$

where

$$\lambda = \frac{t_0}{t_r} \tag{18}$$

is the observational timescale relative to the characteristic surface relaxation timescale. The parameter

$$\nu = \frac{\bar{u}_s t_0}{h_0} \tag{19}$$

is the background sliding velocity relative to the vertical velocity anomaly scale, while

$$\tilde{u}_h = \frac{\bar{u}_h t_0}{H} \tag{20}$$

is the background surface flow speed relative to the characteristic horizontal velocity scale H/t_0, and

$$\tilde{\tau} = \frac{\bar{\tau} H t_0}{2\eta} \tag{21}$$

is the basal stress-gradient parameter relative the characteristic drag $2\eta/H$ produced over the timescale t_0.

Similarly, the basal surface evolution equation (7) scales to

$$\frac{\partial \widehat{s}}{\partial t} + ik_x\tilde{u}_s\widehat{s} = \widehat{w}_b + \widehat{m}, \tag{22}$$

where

$$\tilde{u}_s \equiv \frac{\bar{u}_s t_0}{H} \tag{23}$$

is the background sliding speed relative to the characteristic horizontal velocity scale. We provide values for the nondimensional parameters in Table 1.

2.5 General Solutions

The solution to (17) for the Fourier-transformed elevation anomaly is

$$\widehat{h} = (\widehat{a} + \mathsf{T}_w\widehat{w}_b + ik_x\mathsf{T}_\beta(\nu\widehat{\beta} - \tilde{\tau}\widehat{s})) * \mathsf{K}_h, \tag{24}$$

where the kernel

$$\mathsf{K}_h = \exp\left(-[ik_x\tilde{u}_h + \lambda \mathsf{R}_g]t\right) \tag{25}$$

describes advection and surface relaxation. In deriving (24), we have assumed a spatially uniform initial condition of $h = 0$ for simplicity. The solution (24) also depends on the lower surface elevation s. Integrating equation (22), we obtain

$$\widehat{s} = (\widehat{w}_b + \widehat{m}) * \mathsf{K}_s, \tag{26}$$

$$\mathsf{K}_s = \exp\left(-ik_x\tilde{u}_s t\right). \tag{27}$$

The kernel K_s (eq. 27) describes advection of the lower surface elevation due to sliding at the background flow speed. Substituting the expression for $\widehat{s}$ (eq. 26) into equation (24), we obtain the solution formula

$$\widehat{h} = \left(\widehat{a} + \mathsf{T}_w\widehat{w}_b + ik_x\mathsf{T}_\beta\left(\nu\widehat{\beta} - \tilde{\tau}[(\widehat{w}_b + \widehat{m}) * \mathsf{K}_s]\right)\right) * \mathsf{K}_h. \tag{28}$$

Given perturbations (w_b, β, m, a) as input, we compute the physical-space solution h by applying the inverse Fourier transform (eq. 4) to equation (28).

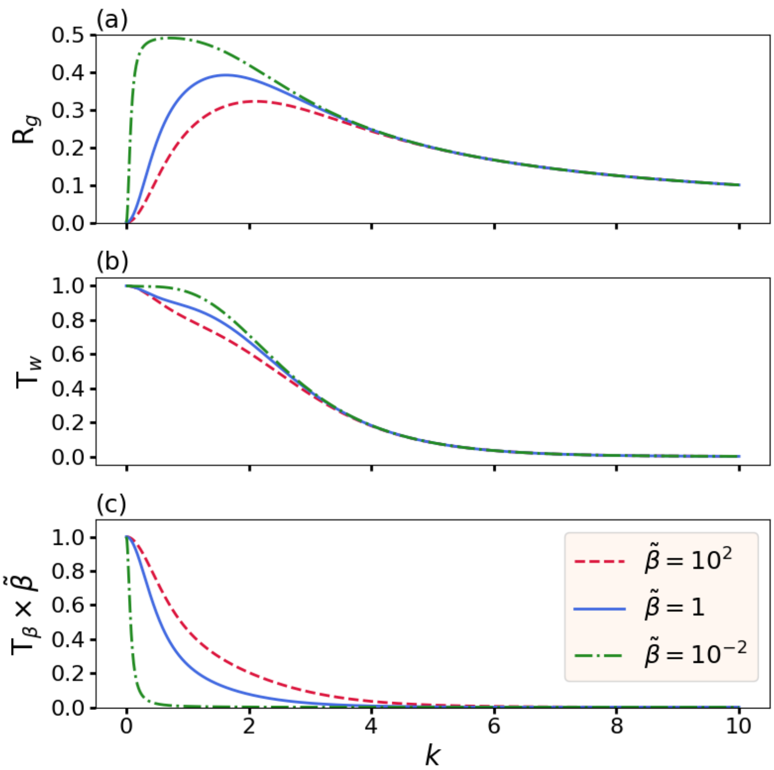

Figure 2. Scaled relaxation and transfer functions over a range of k. (a) Relaxation function (eq. 14) with $c_\alpha = 0$, (b) basal-velocity transfer function (eq. 10), and (c) basal-drag transfer function (eq. 16) for different values of the background drag parameter $\tilde{\beta}$. Panel (c) shows that T_β is bounded above by $\tilde{\beta}^{-1}$.

Table 1. Model parameters and default values. The default values are the same for the examples in Section 4.1 and Section 4.2 except where noted.

Symbol	Definition	Default values	
Dimensional		Section 4.1	Section 4.2
η	ice viscosity	10^{13} Pa s	
g	gravitational acceleration	9.81 m/s^2	
ρ	ice density	917 kg/m^3	
α	background basal slope	0.2°	0°
H	background ice thickness	1000 m	
$\bar{\beta}$	background basal drag coefficient	5×10^9 Pa s/m	
$\bar{u}_h$	background surface speed	∼250 m/yr	0 m/yr
$\bar{u}_s$	background sliding speed	200 m/yr	0 m/yr
$\bar{\tau}$	basal shear stress gradient (eq. 12)	∼47 Pa/m	0 Pa/m
h_0	elevation anomaly scale	1 m	
t_0	observational timescale	1 yr	
w_0	vertical velocity scale	1 m/yr	
t_r	surface relaxation timescale (eq. 15)	$\sim 7 \times 10^{-2}$ yr	
Nondimensional			
λ	t_0/t_r	∼14	
ν	$\bar{u}_s/w_0$	200	0
$\tilde{\tau}$	$\bar{\tau}Ht_0/(2\eta)$	$\sim 7.4 \times 10^{-2}$	0
$\tilde{\beta}$	$\bar{\beta}H/(2\eta)$	0.25	
$\tilde{u}_s$	$\bar{u}_s t_0/H$	0.2	0
$\tilde{u}_h$	$\bar{u}_h t_0/H$	∼0.25	0
T	final time	10	
t_p	oscillation period	10	5
L	domain length and width	80	

3 Inverse Problems

First, we derive inverse methods for inferring a single type of basal perturbation (i.e., either w_b or β) from altimetry data (Section 3.1). We then extend these methods to include horizontal surface velocity data to facilitate inversion for multiple fields (i.e., both w_b and β) or improve altimetry-based inversion results (Section 3.2). For simplicity, we neglect basal melting and surface accumulation perturbations in the inversion examples below by setting $m = 0$ and $a = 0$ in the forward model (eq. 28).

In the following sections, we use variational calculus to derive normal equations that are associated with least-squares optimization problems (Vogel, 2002, ch. 2). To this end, we define the inner products of functions $f_1(x, y, t)$ and $f_2(x, y, t)$ to be

$$\langle f_1, f_2 \rangle = \int_0^T \int_{-\infty}^{+\infty} \int_{-\infty}^{+\infty} f_1 f_2 \, \mathrm{d}x \, \mathrm{d}y \, \mathrm{d}t, \tag{29}$$

where T is the length of the observational time frame. We will also use the norm $\|f\| = \sqrt{\langle f, f \rangle}$ associated with this inner product. The adjoint operators defined below involve cross-correlation over time, which we denote by

$$f_1 \star f_2 = \int_t^T f_1^*(-(t - \tilde{t})) f_2(\tilde{t}) \, \mathrm{d}\tilde{t}, \tag{30}$$

with f^* being the complex conjugate of f. Finally, we will denote the Fourier transform operator and its inverse by $\mathcal{F}$ (eq. 2) and $\mathcal{F}^{-1}$ (eq. 4), respectively.

3.1 Altimetry Inversions

First, we consider the problem of inverting for either w_b or β, given elevation data h^{obs}. Taking the inverse Fourier transform of equation (28), the solution operator $\mathcal{H}_f$ that maps the parameter f (either w_b or β) to the modelled state h takes the form

$$\mathcal{H}_f(f) = \mathcal{F}^{-1}\left(\mathsf{K}_f * \mathcal{F}(f)\right), \tag{31}$$

where the kernel for each parameter is

$$\mathsf{K}_f = \begin{cases} \mathsf{T}_w \mathsf{K}_h - i k_x \mathsf{T}_\beta \tilde{\tau}(\mathsf{K}_s * \mathsf{K}_h) & f = w_b \\ i k_x \nu \mathsf{T}_\beta \mathsf{K}_h & f = \beta \end{cases}. \tag{32}$$

The least-squares solution is found by minimizing the regularized objective functional

$$\mathcal{J}(f) = \frac{1}{2}\|\mathcal{H}_f(f) - h^{\mathrm{obs}}\|^2 + \mathcal{R}(f) \tag{33}$$

where $\mathcal{R}$ is a regularization functional. Supposing that the first variation of (33) vanishes, we obtain the (infinite-dimensional) normal equations

$$\mathcal{H}_f^\dagger(\mathcal{H}_f(f)) + \delta\mathcal{R}(f) = \mathcal{H}_f^\dagger(h^{\mathrm{obs}}), \tag{34}$$

where $\delta\mathcal{R}$ denotes the variational derivative of $\mathcal{R}$ and

$$\mathcal{H}_f^\dagger(f) = \mathcal{F}^{-1}\left(\mathsf{K}_f \star \mathcal{F}(f)\right) \tag{35}$$

is the adjoint of $\mathcal{H}_f$ with respect to the inner product (29).

Provided that $\delta\mathcal{R}$ is linear in f, we can solve (34) with the conjugate gradient method, which generalizes to infinite-dimensional operator equations (Atkinson & Han, 2009, ch. 5). Here, we consider a Tikhonov-type smoothness regularization of the form

$$\mathcal{R}(f) = \frac{\varepsilon}{2}\left(\left\|\frac{\partial f}{\partial x}\right\|^2 + \left\|\frac{\partial f}{\partial y}\right\|^2\right), \tag{36}$$

which has the variational derivative

$$\delta\mathcal{R}(f) = -\varepsilon\left(\frac{\partial^2 f}{\partial x^2} + \frac{\partial^2 f}{\partial y^2}\right) \tag{37}$$

where ε is a regularization parameter.

3.2 Incorporating Velocity Data

We briefly describe two motivations for incorporating horizontal surface velocity anomaly data, $[u^{\text{obs}}, v^{\text{obs}}]^T$, into the inversions. First, equation (28) shows that both vertical velocity and basal drag perturbations can influence the surface elevation anomaly. Simultaneous inversion for both types of perturbations is only feasible if horizontal surface velocity data is available. Second, velocity constraints can improve altimetry-based inversion results even if these are only available at a few Global Positioning System (GPS) stations. We consider both continuously-distributed and discretely-distributed (e.g., from GPS stations) surface velocity data in the formulation below. To cover both cases succintly, we let $[u^{\text{obs}}, v^{\text{obs}}]^T$ denote an interpolation of the data in the case that observations are only available at a discrete set of spatial points.

Expressions for the horizontal surface velocity are derived in the Supporting Information (Text S1) and provided in Appendix A. From equations (A1) and (A2), the (coupled) horizontal surface velocity solution operators take the form

$$\mathcal{U}_c(w_b, \beta) = \mathcal{F}^{-1}\left(-\mathsf{U}_\beta\left[\nu\mathcal{F}(\beta) - \tilde{\tau}\mathcal{F}(w_b) * \mathsf{K}_s\right] - ik_x\left[\lambda\mathsf{U}_h\mathcal{F}(\mathcal{H}_c(w_b, \beta)) + \mathsf{U}_w\mathcal{F}(w_b)\right]\right) \quad (38)$$

$$\mathcal{V}_c(w_b, \beta) = \mathcal{F}^{-1}(-\mathsf{V}_\beta[\nu\mathcal{F}(\beta) - \tilde{\tau}\mathcal{F}(w_b) * \mathsf{K}_s] - ik_y\left[\lambda\mathsf{V}_h\mathcal{F}(\mathcal{H}_c(w_b, \beta)) + \mathsf{V}_w\mathcal{F}(w_b)\right]) \quad (39)$$

where

$$\mathcal{H}_c(w_b, \beta) = \mathcal{H}_{w_b}(w_b) + \mathcal{H}_\beta(\beta) \quad (40)$$

is the (coupled) elevation solution operator. In equations (38) and (39), U_f and V_f are functions describing the velocity anomaly response to perturbations f (h, w_b, and β). Likewise, we define the decoupled velocity solution operators via

$$\mathcal{U}_{w_b}(w_b) = \mathcal{U}_c(w_b, 0), \quad \mathcal{U}_\beta(\beta) = \mathcal{U}_c(0, \beta) \quad (41)$$

$$\mathcal{V}_{w_b}(w_b) = \mathcal{V}_c(w_b, 0), \quad \mathcal{V}_\beta(\beta) = \mathcal{V}_c(0, \beta), \quad (42)$$

which have adjoints given by

$$\mathcal{U}^\dagger_{w_b}(f) = \mathcal{H}^\dagger_{w_b}(\mathcal{F}^{-1}(ik_x\lambda\mathsf{U}^*_h\mathcal{F}(f))) + \mathcal{F}^{-1}(ik_x\mathsf{U}_w\mathcal{F}(f) + \tilde{\tau}\mathcal{F}(f) \star \mathsf{K}_s) \quad (43)$$

$$\mathcal{V}^\dagger_{w_b}(f) = \mathcal{H}^\dagger_{w_b}(\mathcal{F}^{-1}(ik_y\lambda\mathsf{V}^*_h\mathcal{F}(f))) + \mathcal{F}^{-1}(ik_y\mathsf{V}_w\mathcal{F}(f) + \tilde{\tau}\mathcal{F}(f) \star \mathsf{K}_s) \quad (44)$$

$$\mathcal{U}^\dagger_\beta(f) = \mathcal{H}^\dagger_\beta(\mathcal{F}^{-1}(ik_x\lambda\mathsf{U}^*_h\mathcal{F}(f))) - \mathcal{F}^{-1}(\nu\mathsf{U}_\beta\mathcal{F}(f)) \quad (45)$$

$$\mathcal{V}^\dagger_\beta(f) = \mathcal{H}^\dagger_\beta(\mathcal{F}^{-1}(ik_y\lambda\mathsf{V}^*_h\mathcal{F}(f))) - \mathcal{F}^{-1}(\nu\mathsf{V}_\beta\mathcal{F}(f)). \quad (46)$$

The adjoints of the coupled solution operators (38)-(40) are the vector-valued operators

$$\mathcal{U}^\dagger_c(f) = \begin{bmatrix} \mathcal{U}^\dagger_{w_b}(f) \\ \mathcal{U}^\dagger_\beta(f) \end{bmatrix}, \quad \mathcal{V}^\dagger_c(f) = \begin{bmatrix} \mathcal{V}^\dagger_{w_b}(f) \\ \mathcal{V}^\dagger_\beta(f) \end{bmatrix}, \quad \mathcal{H}^\dagger_c(f) = \begin{bmatrix} \mathcal{H}^\dagger_{w_b}(f) \\ \mathcal{H}^\dagger_\beta(f) \end{bmatrix}. \quad (47)$$

To incorporate the velocity data $[u^{\text{obs}}, v^{\text{obs}}]^T$ into the inversions, we consider a weighted multi-objective functional

$$\begin{aligned} \mathcal{J}_c(w_b, \beta) \quad = \quad & \frac{1}{2}\|\mathcal{H}_c(w_b, \beta) - h^{\text{obs}}\|^2 + \frac{1}{2}\langle\chi, |\mathcal{U}_c(w_b, \beta) - u^{\text{obs}}|^2\rangle \\ & + \frac{1}{2}\langle\chi, |\mathcal{V}_c(w_b, \beta) - v^{\text{obs}}|^2\rangle + \mathcal{R}_{w_b}(w_b) + \mathcal{R}_\beta(\beta) \end{aligned} \quad (48)$$

where χ is a weighted state-to-observation map. In the case of N discrete spatial points (x_j, y_j) where velocity data is collected continuously over time, the map χ takes the form

$$\chi(x, y) = \chi_0 \sum_{j=1}^{N} \delta(x - x_j, y - y_j), \quad (49)$$

where δ is the Dirac delta distribution and χ_0 is a scalar weight that determines the strength of the velocity misfit terms relative to the elevation misfit term in the objective functional (48). Restriction of the data misfit to a collection of discrete time steps can be accomplished in a similar way. We also consider the case of velocity data that is distributed continuously in space, in which case $\chi \equiv \chi_0$. In the objective functional (48), we let $\mathcal{R}_{w_b}$ and $\mathcal{R}_\beta$ denote regularizations on w_b and β, respectively.

Supposing that the first variations of (48) with respect to w_b and β vanish, we obtain the system

$$\begin{cases} \mathcal{H}^\dagger_{w_b}(\mathcal{H}_c(w_b,\beta)) + \chi\left[\mathcal{U}^\dagger_{w_b}(\mathcal{U}_c(w_b,\beta)) + \mathcal{V}^\dagger_{w_b}(\mathcal{V}_c(w_b,\beta))\right] + \delta\mathcal{R}_{w_b}(w_b) \\ = \mathcal{H}^\dagger_{w_b}(h^{\text{obs}}) + \chi\left[\mathcal{U}^\dagger_{w_b}(u^{\text{obs}}) + \mathcal{V}^\dagger_{w_b}(v^{\text{obs}})\right] \\ \\ \mathcal{H}^\dagger_{\beta}(\mathcal{H}_c(w_b,\beta)) + \chi\left[\mathcal{U}^\dagger_{\beta}(\mathcal{U}_c(w_b,\beta)) + \mathcal{V}^\dagger_{\beta}(\mathcal{V}_c(w_b,\beta))\right] + \delta\mathcal{R}_{\beta}(\beta) \\ = \mathcal{H}^\dagger_{\beta}(h^{\text{obs}}) + \chi\left[\mathcal{U}^\dagger_{\beta}(u^{\text{obs}}) + \mathcal{V}^\dagger_{\beta}(v^{\text{obs}})\right] \end{cases}. \tag{50}$$

Utilizing the definitions of the adjoint operators (47), we rewrite the system (50) in vectorized form as

$$\begin{aligned} \mathcal{H}^\dagger_c(\mathcal{H}_c(w_b,\beta)) + \chi\left[\mathcal{U}^\dagger_c(\mathcal{U}_c(w_b,\beta)) + \mathcal{V}^\dagger_c(\mathcal{V}_c(w_b,\beta))\right] + \delta\mathcal{R}_c(w_b,\beta) \\ = \mathcal{H}^\dagger_c(h^{\text{obs}}) + \chi\left[\mathcal{U}^\dagger_c(u^{\text{obs}}), +\mathcal{V}^\dagger_c(v^{\text{obs}})\right] \end{aligned} \tag{51}$$

where $\delta\mathcal{R}_c(w_b,\beta) = [\delta\mathcal{R}_{w_b}(w_b), \delta\mathcal{R}_\beta(\beta)]^T$. The solution to (51) is obtained with the conjugate gradient method (Atkinson & Han, 2009, ch. 5).

3.3 Discretization and Implementation

We discretize the problem by defining the grid spacings $\Delta x = L/100$, $\Delta y = L/100$, and $\Delta t = t_p/100$, where L is the domain length in the x and y directions, and t_p is the oscillation period defined below (Section 4). For all experiments herein, we set the domain length to $L = 80$. All Fourier transforms, convolutions, and cross-correlations are computed with fast Fourier transform methods in SciPy (Cooley & Tukey, 1965; Virtanen et al., 2020). We compute inner products (eq. 29) with the trapezoidal rule in our implementation of the conjugate gradient method (Atkinson & Han, 2009, ch. 5). The nondimensional parameters used in the synthetic experiments are provided in Table 1. The code for reproducing the inversion results in Section 4 is openly available (DOI: 10.5281/zenodo.5775178).

4 Results

First, we provide synthetic test problems for altimetry-based inversions (Section 4.1.1) and joint velocity-altimetry inversions (Section 4.1.2) with synthetic data produced by the small-perturbation model. Then, we attempt to invert synthetic data from a nonlinear subglacial lake model to assess the validity of the method when applied to more complex data (Section 4.2). Throughout, we use the notation $\|f\|_\infty$ to denote the maximum absolute value of a function f over space and time.

4.1 Synthetic Data from the Linearized Model

4.1.1 Altimetry-based Inversions

We first consider two synthetic test problems to illustrate the altimetry-based inverse methods derived in Section 3.1. Motivated by subglacial lake filling-draining cycles, we first consider a smooth (Gaussian-shaped) basal vertical velocity anomaly that oscillates in time. The synthetic data h^{obs} for this problem is produced by providing the

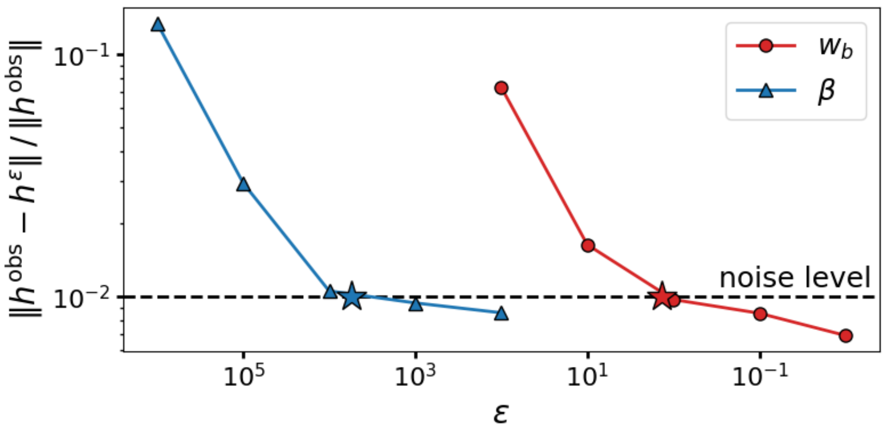

Figure 3. Discrepancy diagram showing estimation of optimal regularization parameters ε (stars) for each synthetic test problem, where h^{ε} denotes the modelled elevation anomaly for a particular value of ε. The noise level is shown by a dashed line. The optimal parameters are $\varepsilon \approx 1.3$ for the w_b inversion and $\varepsilon \approx 5.5 \times 10^3$ for the β inversion.

true solution

$$w_b^{\text{true}}(x,y,t) = 5\exp\left(-\frac{x^2+y^2}{2\sigma^2}\right)\sin(2\pi t/t_p) \tag{52}$$

with $t_p = T$ as input to the forward model (eq. 28) and then adding a small amount of Gaussian white noise to the modelled elevation (Figure 3). We set the standard deviation of the Gaussian anomaly in the true solution (eq. 52) to $\sigma = 20/3$. For this input (eq. 52), the synthetic elevation data h^{obs} is also roughly Gaussian-shaped and oscillates in time (Figure 4a-4c).

The arrival of subglacial water can also produce a basal drag anomaly. Therefore, for the second synthetic test we consider a slippery spot that emerges at time $t = T/4$ and disappears after $t = 3T/4$, given by

$$\beta^{\text{true}}(x,y,t) = -(8\times 10^{-2})\exp\left(-\frac{x^2+y^2}{2\sigma^2}\right)B(t), \tag{53}$$

where B is a continuous box-type function,

$$B(t) = \begin{cases} \sin(2\pi\, t\,\mathrm{sgn}(\frac{T}{2}-t)/T) & |t-\frac{T}{2}| \geq \frac{T}{4} \\ 1 & |t-\frac{T}{2}| < \frac{T}{4} \end{cases}, \tag{54}$$

that controls the appearance and disappearance of the anomaly. As before, we set the standard deviation in the true solution (53) to $\sigma = 20/3$ and add a small amount of noise to the modelled elevation to produce the synthetic data h^{obs}. The synthetic data h^{obs} (Figure 5a-5c) associated with this input (eq. 53) is a dipole where thinning and thickening occur at the upstream and downstream ends of the anomaly, respectively (cf. O. V. Sergienko et al., 2007; O. V. Sergienko & Hulbe, 2011).

For both problems, we apply the discrepancy principle to estimate the optimal regularization parameter ε that minimizes the difference between the modelled and observed elevations without overfitting the data (Figure 3). We provide inversion results for both problems using these optimal regularization parameters. We also show the horizontal surface velocity anomalies for reference, although these data are not used in the inversions (Figures 4 and 5). The inverse method accurately recovers the basal vertical velocity anomaly

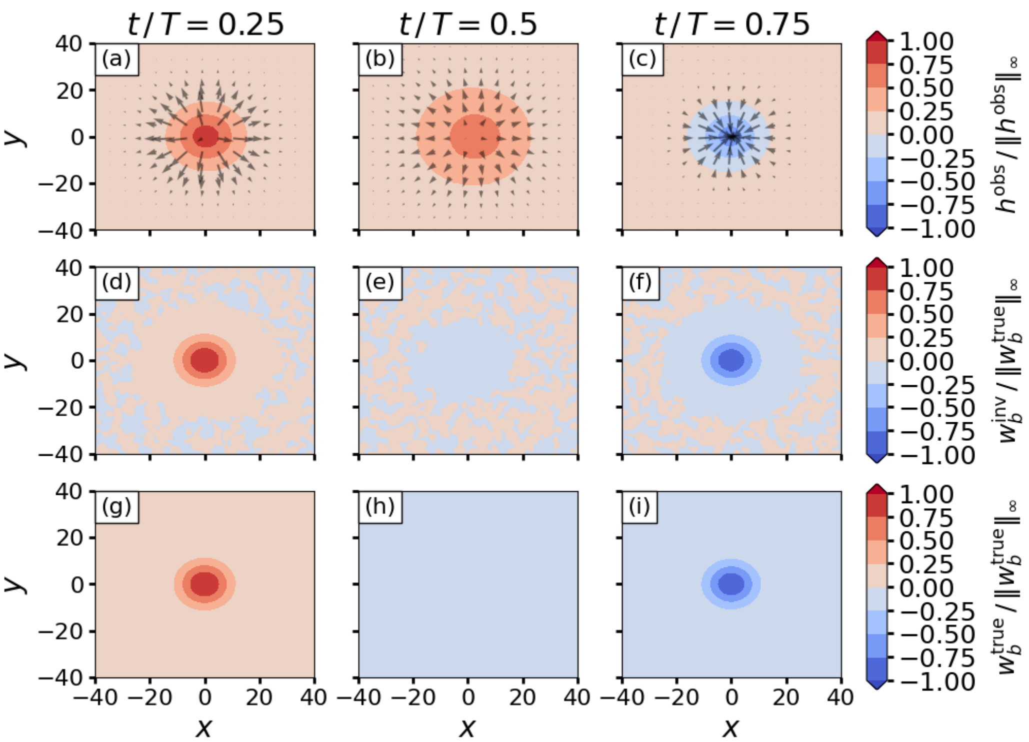

Figure 4. Synthetic test problem of inverting altimetry data for an oscillating basal vertical velocity anomaly (w_b). (a)-(c) Synthetic elevation anomaly data (h^{obs}) contours at three time steps, normalized by its maximum absolute value $\|h^{\mathrm{obs}}\|_\infty \approx 4$. The horizontal surface velocity anomalies are shown as gray arrows that have been normalized by the maximum flow speed ($\sim$13.6). (d)-(f) Basal vertical velocity inversion (w_b^{inv}) at the same time steps, normalized by the maximum absolute value of the true solution (w_b^{true}). (g)-(i) Normalized true solution where $\|w_b^{\mathrm{true}}\|_\infty = 5$. The regularization parameter used here is the optimal value shown in Figure 3. Movie S1 shows the inversion at each time step.

over the entire observational time frame up to a small-amplitude component from the noise in the data (Figure 4 and Movie S1). While the basal drag inversion predicts the correct shape and order of magnitude of the anomaly, the amplitude and areal extent are both underestimated (Figure 5 and Movie S2). This underestimation is not sensitive to the discretization details, noise level, or stopping tolerance of the conjugate gradient solver. Instead, this discrepancy reflects a lack of continuous dependence that is common in inverse problems (Vogel, 2002; Hanke, 2017). In other words, the basal drag inversion produces an elevation anomaly that closely matches the data even though it deviates from the "true" basal drag (cf. Habermann et al., 2012). Below, we show that incorporation of horizontal surface velocity data as additional constraints can remedy this problem.

4.1.2 Joint Velocity-Altimetry Inversions

First, we seek to refine the basal drag coefficient inversion by incorporating velocity data at a discrete collection of spatial points that represent synthetic GPS stations. In this case, the state-to-observation map is given by equation (49) where we set $\chi_0 = 10^{-3}$ to avoid giving undue weight to the pointwise velocity measurements. We assume

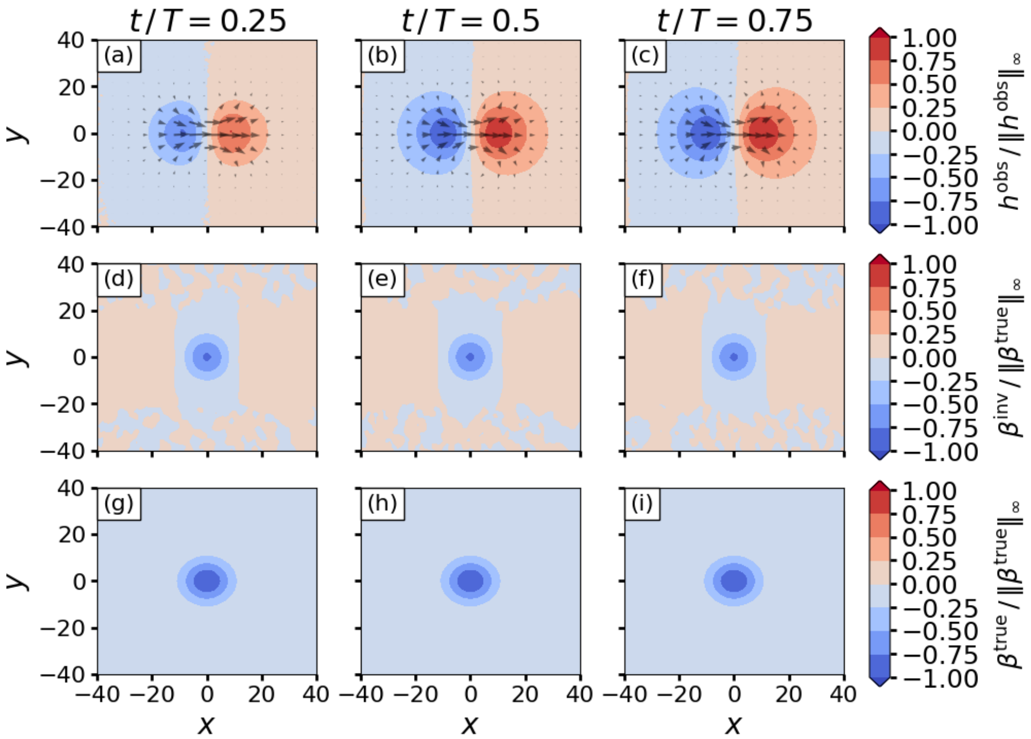

Figure 5. Synthetic test problem of inverting altimetry data for a slippery spot (β). (a)-(c) Synthetic elevation anomaly data (h^{obs}) contours at three time steps, normalized by its maximum absolute value $\|h^{\text{obs}}\|_\infty \approx 2.87$. The horizontal surface velocity anomalies are shown as gray arrows that have been normalized by the maximum flow speed ($\sim$33.3). (d)-(f) Basal drag coefficient inversion (β^{inv}) at the same time steps, normalized by the maximum absolute value of the true solution (β^{true}). (g)-(i) Normalized true solution where $\|\beta^{\text{true}}\|_\infty = 0.08$. The regularization parameter used here is the optimal value shown in Figure 3. Movie S2 shows the inversion at each time step.

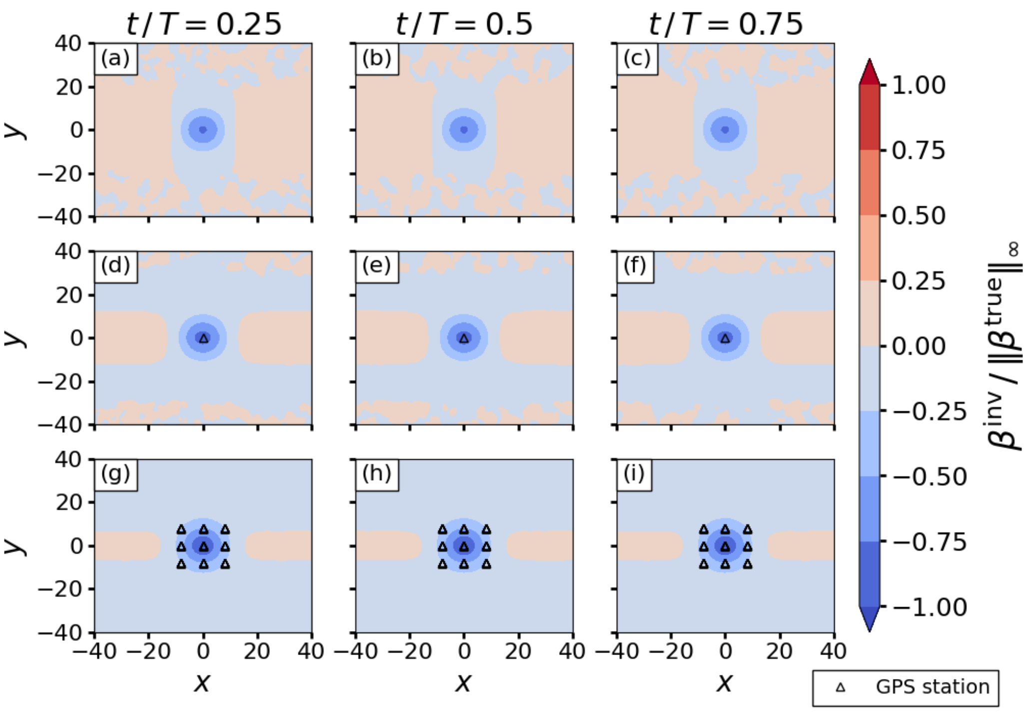

Figure 6. Same synthetic test problem as in Figure 5, except for the incorporation of velcity data from synthetic GPS stations (black triangles). The velocity field is shown in Figure 5a-5c. Inversion results are shown for (a)-(c) no stations, (d)-(f) one station, and (g)-(i) an array of nine stations. The inversions have been normalized by the maximum absolute value of the true solution ($\|\beta^{\mathrm{true}}\|_\infty = 0.08$, Figure 5g-5i). The regularization parameter used here is the optimal value shown in Figure 3.

the same true solution β^{true} and synthetic elevation data as in Section 4.1 (Figure 5). The synthetic horizontal surface velocity data is shown in Figure 5a-5c. Relative to an inversion with no GPS stations (Figure 6a-6c), we find that placing a single GPS station over the anomaly results in a slight improvement in the amplitude and areal extent of the inversion (Figure 6d-6f) while placing an array of nine stations results in a modest improvement (Figure 6g-6i).

Accurate reconstruction of overlapping vertical velocity and basal drag anomalies is feasible if horizontal surface velocity and altimetry data are both available at high spatial and temporal resolution. To illustrate this, we suppose that the elevation and surface velocity perturbations are produced by an oscillating subglacial lake (eq. 52) that coincides with a slippery spot (eq. 53). In this case, we set the state-to-observation map to $\chi \equiv \chi_0$ with $\chi_0 = 10^{-1}$ so that the elevation and velocity misfit terms in (48) are approximately balanced for these data. We obtain accurate reconstructions of both the basal drag and vertical velocity anomalies over the observational time frame (Figure 7 and Movie S3).

4.2 Synthetic Data from a Nonlinear Model

To assess the applicability of the inverse method to more complex data, we attempt to invert synthetic data produced by a nonlinear model for subglacial lake oscillations (Supporting Information Text S2). In contrast to the linearized model, the nonlinear model

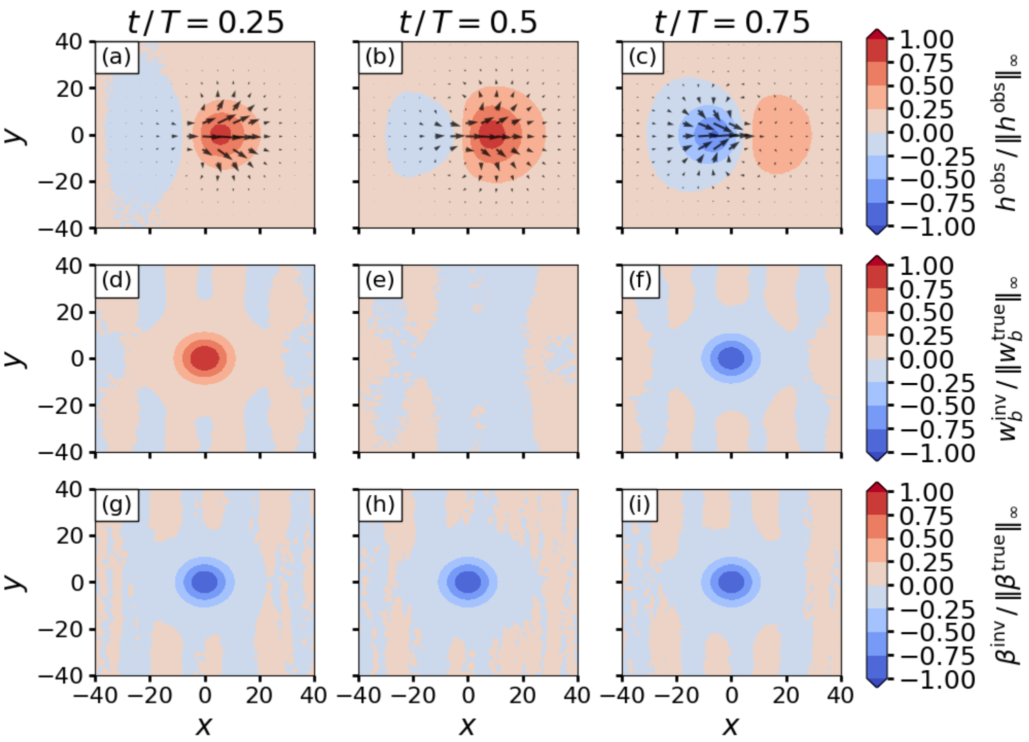

Figure 7. Synthetic test problem of inverting altimetry and horizontal surface velociy data for an oscillating vertical velocity anomaly (w_b) that coincides with a slippery spot (β). (a)-(c) Synthetic elevation anomaly data (h^{obs}) contours at three time steps, normalized by its maximum absolute value $\|h^{\mathrm{obs}}\|_\infty \approx 5.6$. The horizontal surface velocity anomalies $[u^{\mathrm{obs}}, v^{\mathrm{obs}}]^T$ are shown as black arrows that are normalized by the maximum flow speed ($\sim$38.9). (d)-(f) Basal vertical velocity inversion (w_b^{inv}), normalized by the maximum absolute value of the true solution (w_b^{true}, Figure 4g-4i). (g)-(i) Basal drag coefficient inversion (β^{inv}), normalized by the maximum absolute value of the true solution (β^{true}, Figure 5g-5i). The regularization parameters used here are the optimal values shown in Figure 3. Movie S3 shows the inversion at each time step.

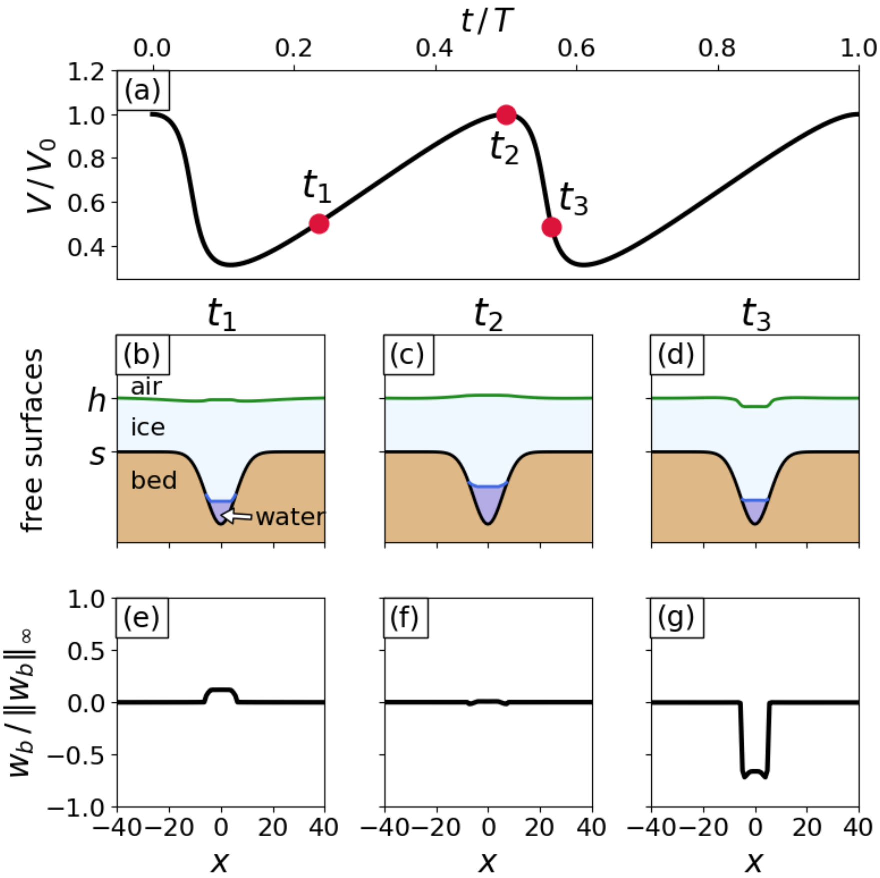

Figure 8. Synthetic data and basal vertical velocity from a nonlinear subglacial lake model in one horizontal dimension. (a) Subglacial lake water volume V time series normalized by the initial water volume V_0. The times t_1, t_2, and t_3 are the time steps shown in (b)-(g). (b)-(d) Cross-sections depicting the free surfaces (h and s) at time steps t_1 to t_3. The atmosphere, ice, water, and bed are noted in (b). For reference, the maximum elevation anomaly is ∼1.4m and the bed trough is 8m deep in dimensional terms. (e)-(g) Basal vertical velocity (w_b) from the nonlinear model at time steps t_1 to t_3 normalized by its maximum absolute value ($\|w_b\|_\infty \approx 6.58$). Movie S4 shows the simulation at each time step.

assumes a viscosity following Glen's law (Cuffey & Paterson, 2010; Glen, 1955), a water-volume change constraint at the lower boundary rather than a prescribed vertical velocity anomaly, and fully nonlinear surface kinematic equations (Stubblefield, Creyts, et al., 2021; Stubblefield, Spiegelman, & Creyts, 2021). Motivated by oscillation patterns observed on the Whillans and Mercer ice streams in West Antarctica (Fricker & Scambos, 2009; Siegfried et al., 2016; Siegfried & Fricker, 2018, 2021), we assume a sawtooth water-volume time series with a period of $t_p = 5$ (Figure 8a). Figure 8 and Movie S4 show the elevation from the nonlinear model and the associated basal vertical velocity field over time. As the nonlinear model results are in one horizontal dimension (i.e., the x direction), we extend the synthetic data to two horizontal dimensions by assuming no variation in the y direction. The code for reproducing this synthetic data is openly available (DOI: 10.5281/zenodo.5775182).

To facilitate a straightforward comparison, we assume that the background state parameters between the nonlinear and linearized model are the same with the caveats that (i) the basal drag vanishes over the lake in the nonlinear model and (ii) the zero strain-rate viscosity in the nonlinear model coincides with the linearized model viscosity (Supporting Information Text S2). We assume a purely cryostatic background state with $\alpha = 0$ and $\bar{u} \equiv 0$ to limit the influence of this basal drag transition on the elevation change, allowing inversion for the basal vertical velocity with altimetry data alone (Table 1).

The inverse method is able to recover the basal vertical velocity from the nonlinear model despite the simplifying assumptions in the small-perturbation approach (Figure 9 and Movie S5). The main discrepancies are that the inversion can overestimate the areal extent and underestimate the magnitude of the nonlinear model anomaly. However, these discrepancies appear to be relatively small for this example. While the total subglacial lake water volume V cannot be estimated unless the initial volume V_0 is known, the volume change time series $\Delta V = V - V_0$ can be estimated from the inversion via

$$\Delta V(t) = \int_0^t \int_{-\frac{L}{2}}^{+\frac{L}{2}} w_b(x, \tilde{t}\,)\, \mathrm{d}x\, \mathrm{d}\tilde{t}. \tag{55}$$

Equation (55) follows from the basal surface evolution equation (22) when the background sliding speed $\tilde{u}_s$ and basal melt rate anomaly m are zero. The timing and magnitude of the inverted volume change agrees quite well with the true volume change (Figure 9a).

5 Discussion

The altimetry-based inverse methods developed herein can quantify a variety of subglacial phenomena, including subglacial lake activity, slippery or sticky spots, and anomalous bed topography. Inversion for a single parameter field is feasible with altimetry data alone (Figures 4, 5, and 9). However, overlapping basal vertical velocity and drag anomalies are likely to be common because active subglacial lakes or bed topography can potentially produce both types of perturbations (e.g., Gudmundsson & Raymond, 2008; O. V. Sergienko et al., 2007). We have shown that incorporating surface velocity data with high spatial and temporal resolution into the inversions facilitates simultaneous estimation of basal drag and vertical velocity perturbations (Figure 7). Therefore, joint velocity-altimetry inversions are a promising approach for determining the relative influence of each perturbation type in regions where hydrologic or topographic anomalies are associated with basal sliding variations.

The altimetry-based inverse methods developed herein complement existing velocity-based inverse methods. For example, our altimetry-based inversions rely on knowledge of the background flow state (i.e., basal drag and viscosity), which can be estimated with existing velocity-based methods (e.g., Arthern et al., 2015; Morlighem et al., 2010, 2013; Petra et al., 2012). Furthermore, the methods developed herein are intended for targeted study of localized elevation anomalies like those produced by subglacial lakes rather than

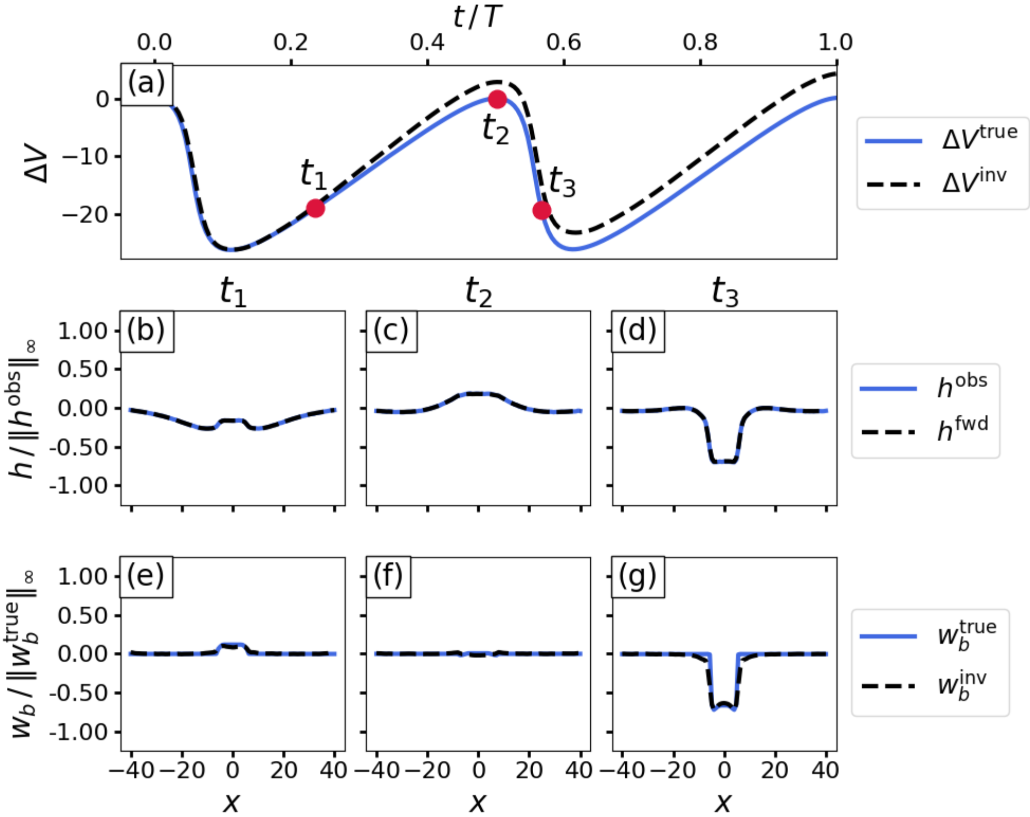

Figure 9. Inversion of synthetic data from the nonlinear subglacial lake model shown in Figure 8. (a) Time series of the true volume change ΔV^{true} compared to the volume change estimated from the inversion ΔV^{inv} (eq. 55). The times t_1, t_2, and t_3 are the time steps shown in (b)-(g). (b)-(d) Synthetic data (h^{obs}) and modelled elevation ($h^{\mathrm{fwd}} = \mathcal{H}_{w_b}(w_b^{\mathrm{inv}})$) associated with the inversion. The elevations are normalized by the maximum absolute value of the data ($\|h^{\mathrm{obs}}\|_\infty \approx 1.42$). (e)-(g) Basal vertical velocity from the nonlinear model (w_b^{true}) and the inversion (w_b^{inv}) normalized by the maximum absolute value of the true solution ($\|w_b^{\mathrm{true}}\|_\infty \approx 6.58$). The optimal regularization parameter for this example is $\varepsilon \approx 5 \times 10^{-2}$. Movie S5 shows the inversion at each time step.

ice-sheet-scale inversions. In the absence of surface velocity data with high spatial resolution, these altimetry-based inverse methods are a simple way to quantify the source of elevation anomalies that are predominantly caused by a single type of basal perturbation (Figures 4 and 5). Moreover, we have shown that incorporation of GPS data from a handful of stations can improve the inversion results (Figure 6). Developing a framework for optimizing the placement of GPS stations over ice-sheet elevation anomalies would be valuable for future campaigns targeting subglacial phenomena.

In this study, we have only used a Tikhonov-type smoothness regularization that leads to a linear inverse problem. Alternative regularizations, such as total variation (e.g., Strong & Chan, 2003) or L^1 sparsity-promoting (e.g., Stadler, 2009) regularizations, can be used to more accurately reconstruct sharp boundaries like those in the nonlinear synthetic data (Figure 8e-8g). While we have shown that there is good agreement between the small-perturbation model and the nonlinear subglacial lake model for the example herein, the inversion is smooth and can overshoot the areal extent of the true basal anomaly when there are sharp boundaries (Figure 9g). This overshooting could potentially also cause discrepancies between the true and estimated water-volume change (Figure 9a). Implementing nonlinear regularizations and solving the associated optimization problem with Newton's method could be valuable for refining the detection of subglacial lake boundaries and the estimation of water-volume changes.

The primary limitations of these perturbation-based inverse methods are the restriction of the forward model to a linear rheology, linear sliding law, and geometrically simple spatial domain. While these limitations are inherent to the solution method used herein, the synthetic test with data from the nonlinear subglacial lake model (Section 4.2) suggests that a Newtonian viscosity and simplified domain are valid approximations for inverting elevation anomalies produced by similar lake oscillations. Incorporating altimetry data into time-dependent full-Stokes inversions that rely on alternative solution methods such as finite elements would be valuable for overcoming these limitations, perhaps relying on neural networks for computational efficiency (e.g., Brinkerhoff et al., 2021; Riel et al., 2021). Moreover, extending these inverse problems to a Bayesian formulation could help to quantify uncertainty in the inversions and background state parameters (Bui-Thanh et al., 2013; Petra et al., 2014; Sullivan, 2015). Finally, these inverse methods could also be extended to estimate melting or freezing rates beneath floating ice shelves. We leave this extension for future work because the ice-shelf problem must be regularized to remove singularities in the long-wavelength limit, which requires a rigorous analysis of the forward model (Bassis & Ma, 2015).

6 Conclusions

Here, we have derived and tested inverse methods for reconstructing time-varying subglacial perturbations from altimetry data. The method accurately reconstructs basal vertical velocity perturbations that can result from subglacial lake activity. While the altimetry-based basal drag inversion is less accurate in terms of matching the true solution, it still characterizes the order of magnitude and shape of the perturbation. Moreover, incorporation of GPS data as additional constraints can remedy this discrepancy. Accurate, simultaneous reconstruction of both basal perturbation types is feasible when horizontal surface velocity data is available at high spatial and temporal resolution. Finally, we have validated the small-perturbation approach by inverting synthetic data from a nonlinear subglacial lake model to obtain a basal vertical velocity field and water volume change time series that agree well with the nonlinear model. These methods hold promise for uncovering the causes of time-varying ice-surface elevation perturbations and elucidating the links between subglacial hydrology, bed properties, and fast ice flow.

Data Availability Statement

No new data was used in this study. The code for reproducing the inversion results (Figures 3-7, 9) is openly available (DOI: 10.5281/zenodo.5775178). The code for running the nonlinear model and producing Figure 8 is also openly available (DOI: 10.5281/zenodo.5775182).

Acknowledgments

A.G.S. was supported by a National Science Foundation Graduate Research Fellowship. A.G.S. is grateful for comments from Marc Spiegelman, Jonathan Kingslake, and Meredith Nettles (LDEO) on an earlier version of the manuscript.

References

Abdalati, W., Zwally, H. J., Bindschadler, R., Csatho, B., Farrell, S. L., Fricker, H. A., ... others (2010). The ICESat-2 laser altimetry mission. *Proceedings of the IEEE*, *98*(5), 735–751.

Achberger, A. M., Christner, B. C., Michaud, A. B., Priscu, J. C., Skidmore, M. L., Vick-Majors, T. J., ... Tulaczyk, S. (2016). Microbial community structure of subglacial Lake Whillans, West Antarctica. *Frontiers in Microbiology*, *7*(SEP), 1–13. doi: 10.3389/fmicb.2016.01457

Arthern, R. J., & Gudmundsson, G. H. (2010). Initialization of ice-sheet forecasts viewed as an inverse robin problem. *Journal of Glaciology*, *56*(197), 527–533.

Arthern, R. J., Hindmarsh, R. C., & Williams, C. R. (2015). Flow speed within the Antarctic ice sheet and its controls inferred from satellite observations. *Journal of Geophysical Research: Earth Surface*, *120*(7), 1171–1188.

Atkinson, K., & Han, W. (2009). *Theoretical numerical analysis* (3rd ed., Vol. 39). Springer.

Balise, M. J., & Raymond, C. F. (1985). Transfer of basal sliding variations to the surface of a linearly viscous glacier. *Journal of Glaciology*, *31*(109), 308–318.

Bassis, J. N., & Ma, Y. (2015). Evolution of basal crevasses links ice shelf stability to ocean forcing. *Earth and Planetary Science Letters*, *409*, 203–211.

Bell, R. E., Studinger, M., Shuman, C. A., Fahnestock, M. A., & Joughin, I. (2007). Large subglacial lakes in East Antarctica at the onset of fast-flowing ice streams. *Nature*, *445*(7130), 904–907. doi: 10.1038/nature05554

Bowling, J., Livingstone, S., Sole, A., & Chu, W. (2019). Distribution and dynamics of Greenland subglacial lakes. *Nature communications*, *10*(1), 1–11.

Brinkerhoff, D., Aschwanden, A., & Fahnestock, M. (2021). Constraining subglacial processes from surface velocity observations using surrogate-based Bayesian inference. *Journal of Glaciology*, *67*(263), 385–403.

Budd, W. (1970). Ice flow over bedrock perturbations. *Journal of Glaciology*, *9*(55), 29–48.

Bui-Thanh, T., Ghattas, O., Martin, J., & Stadler, G. (2013). A computational framework for infinite-dimensional Bayesian inverse problems Part I: The linearized case, with application to global seismic inversion. *SIAM Journal on Scientific Computing*, *35*(6), A2494–A2523.

Christner, B. C., Priscu, J. C., Achberger, A. M., Barbante, C., Carter, S. P., Christianson, K., ... others (2014). A microbial ecosystem beneath the West Antarctic ice sheet. *Nature*, *512*(7514), 310–313.

Cooley, J. W., & Tukey, J. W. (1965). An algorithm for the machine calculation of complex fourier series. *Mathematics of computation*, *19*(90), 297–301.

Cuffey, K. M., & Paterson, W. S. B. (2010). *The physics of glaciers.* Academic Press.

Fricker, H. A., & Scambos, T. (2009). Connected subglacial lake activity on lower Mercer and Whillans Ice Streams, West Antarctica, 2003-2008. *Journal of*

Glaciology, *55*(190), 303–315. doi: 10.3189/002214309788608813

Fricker, H. A., Scambos, T., Bindschadler, R., & Padman, L. (2007). An active subglacial water system in West Antarctica mapped from space. *Science*, *315*(5818), 1544–1548.

Fricker, H. A., Scambos, T., Carter, S., Davis, C., Haran, T., & Joughin, I. (2010). Synthesizing multiple remote-sensing techniques for subglacial hydrologic mapping: application to a lake system beneath MacAyeal Ice Stream, West Antarctica. *Journal of Glaciology*, *56*(196), 187–199.

Fricker, H. A., Siegfried, M. R., Carter, S. P., & Scambos, T. A. (2016). A decade of progress in observing and modeling Antarctic subglacial water systems. *Philosophical Transactions of the Royal Society A: Mathematical, Physical and Engineering Sciences*, *374*(2059). doi: 10.1098/rsta.2014.0294

Glen, J. W. (1955). The creep of polycrystalline ice. *Proceedings of the Royal Society of London. Series A. Mathematical and Physical Sciences*, *228*(1175), 519–538.

Goldberg, D., & Heimbach, P. (2013). Parameter and state estimation with a time-dependent adjoint marine ice sheet model. *The Cryosphere*, *7*(6), 1659–1678.

Goldberg, D., Heimbach, P., Joughin, I., & Smith, B. (2015). Committed retreat of smith, pope, and kohler glaciers over the next 30 years inferred by transient model calibration. *The Cryosphere*, *9*(6), 2429–2446.

Goldberg, D. N., & Sergienko, O. V. (2011). Data assimilation using a hybrid ice flow model. *The Cryosphere*, *5*(2), 315–327.

Gray, L., Joughin, I., Tulaczyk, S., Spikes, V. B., Bindschadler, R., & Jezek, K. (2005). Evidence for subglacial water transport in the West Antarctic Ice Sheet through three-dimensional satellite radar interferometry. *Geophysical Research Letters*, *32*(3), L03501.

Greve, R., & Blatter, H. (2009). *Dynamics of ice sheets and glaciers.* Springer Science & Business Media.

Gudmundsson, G. H. (2003). Transmission of basal variability to a glacier surface. *Journal of Geophysical Research: Solid Earth*, *108*(B5).

Gudmundsson, G. H., Raymond, C. F., & Bindschadler, R. (1998). The origin and longevity of flow stripes on Antarctic ice streams. *Annals of Glaciology*, *27*, 145–152.

Gudmundsson, G. H., & Raymond, M. (2008). On the limit to resolution and information on basal properties obtainable from surface data on ice streams. *The Cryosphere*, *2*(2), 167–178.

Habermann, M., Maxwell, D., & Truffer, M. (2012). Reconstruction of basal properties in ice sheets using iterative inverse methods. *Journal of Glaciology*, *58*(210), 795–808.

Hanke, M. (2017). *A taste of inverse problems: Basic theory and examples.* SIAM.

Hutter, K., Legerer, F., & Spring, U. (1981). First-order stresses and deformations in glaciers and ice sheets. *Journal of Glaciology*, *27*(96), 227–270.

Joughin, I., MacAyeal, D. R., & Tulaczyk, S. (2004). Basal shear stress of the ross ice streams from control method inversions. *Journal of Geophysical Research: Solid Earth*, *109*(B9).

Larour, E., Utke, J., Csatho, B., Schenk, A., Seroussi, H., Morlighem, M., . . . Khazendar, A. (2014). Inferred basal friction and surface mass balance of the Northeast Greenland Ice Stream using data assimilation of ICESat (Ice Cloud and land Elevation Satellite) surface altimetry and ISSM (Ice Sheet System Model). *The Cryosphere*, *8*(6), 2335–2351.

Livingstone, S. J., Sole, A. J., Storrar, R. D., Harrison, D., Ross, N., & Bowling, J. (2019). Brief communication: Subglacial lake drainage beneath Isunguata Sermia, West Greenland: Geomorphic and ice dynamic effects. *The Cryosphere*, *13*(10), 2789–2796.

MacAyeal, D. R. (1993). A tutorial on the use of control methods in ice-sheet modeling. *Journal of Glaciology*, *39*(131), 91–98.
MacAyeal, D. R., Bindschadler, R. A., & Scambos, T. A. (1995). Basal friction of ice stream E, West Antarctica. *Journal of Glaciology*, *41*(138), 247–262.
Markus, T., Neumann, T., Martino, A., Abdalati, W., Brunt, K., Csatho, B., ... others (2017). The Ice, Cloud, and land Elevation Satellite-2 (ICESat-2): science requirements, concept, and implementation. *Remote sensing of environment*, *190*, 260–273.
Morlighem, M., Rignot, E., Seroussi, H., Larour, E., Ben Dhia, H., & Aubry, D. (2010). Spatial patterns of basal drag inferred using control methods from a full-Stokes and simpler models for Pine Island Glacier, West Antarctica. *Geophysical Research Letters*, *37*(14).
Morlighem, M., Seroussi, H., Larour, E., & Rignot, E. (2013). Inversion of basal friction in Antarctica using exact and incomplete adjoints of a higher-order model. *Journal of Geophysical Research: Earth Surface*, *118*(3), 1746–1753.
Mosbeux, C., Gillet-Chaulet, F., & Gagliardini, O. (2016). Comparison of adjoint and nudging methods to initialise ice sheet model basal conditions. *Geoscientific Model Development*, *9*(7), 2549–2562.
Neckel, N., Franke, S., Helm, V., Drews, R., & Jansen, D. (2021). Evidence of Cascading Subglacial Water Flow at Jutulstraumen Glacier (Antarctica) Derived From Sentinel-1 and ICESat-2 Measurements. *Geophysical Research Letters*, *48*(20), e2021GL094472.
Petra, N., Martin, J., Stadler, G., & Ghattas, O. (2014). A computational framework for infinite-dimensional Bayesian inverse problems, Part II: Stochastic Newton MCMC with application to ice sheet flow inverse problems. *SIAM Journal on Scientific Computing*, *36*(4), A1525–A1555.
Petra, N., Zhu, H., Stadler, G., Hughes, T. J., & Ghattas, O. (2012). An inexact Gauss-Newton method for inversion of basal sliding and rheology parameters in a nonlinear Stokes ice sheet model. *Journal of Glaciology*, *58*(211), 889–903. doi: 10.3189/2012JoG11J182
Ranganathan, M., Minchew, B., Meyer, C. R., & Gudmundsson, G. H. (2021). A new approach to inferring basal drag and ice rheology in ice streams, with applications to West Antarctic ice streams. *Journal of Glaciology*, *67*(262), 229–242.
Reeh, N. (1987). Steady-state three-dimensional ice flow over an undulating base: first-order theory with linear ice rheology. *Journal of Glaciology*, *33*(114), 177–185.
Riel, B., Minchew, B., & Bischoff, T. (2021). Data-Driven Inference of the Mechanics of Slip Along Glacier Beds Using Physics-Informed Neural Networks: Case study on Rutford Ice Stream, Antarctica. *Journal of Advances in Modeling Earth Systems*, *n/a*(n/a), e2021MS002621. doi: https://doi.org/10.1029/2021MS002621
Scambos, T. A., Berthier, E., & Shuman, C. A. (2011). The triggering of subglacial lake drainage during rapid glacier drawdown: Crane Glacier, Antarctic Peninsula. *Annals of Glaciology*, *52*(59), 74–82. doi: 10.3189/172756411799096204
Sergienko, O. (2012). The effects of transverse bed topography variations in ice-flow models. *Journal of Geophysical Research: Earth Surface*, *117*(F3).
Sergienko, O. V., & Hulbe, C. L. (2011). 'Sticky spots' and subglacial lakes under ice streams of the Siple Coast, Antarctica. *Annals of Glaciology*, *52*(58), 18–22.
Sergienko, O. V., MacAyeal, D. R., & Bindschadler, R. A. (2007). Causes of sudden, short-term changes in ice-stream surface elevation. *Geophysical Research Letters*, *34*(22), 1–6. doi: 10.1029/2007GL031775
Shapero, D. R., Joughin, I. R., Poinar, K., Morlighem, M., & Gillet-Chaulet, F. (2016). Basal resistance for three of the largest Greenland outlet glaciers.

Journal of Geophysical Research: Earth Surface, *121*(1), 168–180.

Siegfried, M. R., & Fricker, H. A. (2018). Thirteen years of subglacial lake activity in Antarctica from multi-mission satellite altimetry. *Annals of Glaciology*, *59*, 1–14. doi: 10.1017/aog.2017.36

Siegfried, M. R., & Fricker, H. A. (2021). Illuminating active subglacial lake processes with ICESat-2 laser altimetry. *Geophysical Research Letters*, *In press*.

Siegfried, M. R., Fricker, H. A., Carter, S. P., & Tulaczyk, S. (2016). Episodic ice velocity fluctuations triggered by a subglacial flood in West Antarctica. *Geophysical Research Letters*, *43*(6), 2640–2648. doi: 10.1002/2016GL067758

Smith, B. E., Fricker, H. A., Joughin, I. R., & Tulaczyk, S. (2009). An inventory of active subglacial lakes in Antarctica detected by ICESat (2003–2008). *Journal of Glaciology*, *55*(192), 573–595.

Stadler, G. (2009). Elliptic optimal control problems with L1-control cost and applications for the placement of control devices. *Computational Optimization and Applications*, *44*(2), 159.

Stearns, L. A., Smith, B. E., & Hamilton, G. S. (2008). Increased flow speed on a large east antarctic outlet glacier caused by subglacial floods. *Nature Geoscience*, *1*(12), 827–831. doi: 10.1038/ngeo356

Strong, D., & Chan, T. (2003). Edge-preserving and scale-dependent properties of total variation regularization. *Inverse problems*, *19*(6), S165.

Stubblefield, A. G., Creyts, T. T., Kingslake, J., Siegfried, M. R., & Spiegelman, M. (2021). Surface Expression and Apparent Timing of Subglacial Lake Oscillations Controlled by Viscous Ice Flow. *Geophysical Research Letters*, *48*(17), e2021GL094658. (e2021GL094658 2021GL094658) doi: https://doi.org/10.1029/2021GL094658

Stubblefield, A. G., Spiegelman, M., & Creyts, T. T. (2021). Variational formulation of marine ice-sheet and subglacial-lake grounding-line dynamics. *Journal of Fluid Mechanics*, *919*, A23. doi: 10.1017/jfm.2021.394

Sullivan, T. J. (2015). *Introduction to uncertainty quantification* (Vol. 63). Springer.

Thorsteinsson, T., Raymond, C. F., Gudmundsson, G. H., Bindschadler, R. A., Vornberger, P., & Joughin, I. (2003). Bed topography and lubrication inferred from surface measurements on fast-flowing ice streams. *Journal of Glaciology*, *49*(167), 481–490.

Turcotte, D. L., & Schubert, G. (2002). *Geodynamics*. Cambridge university press.

Vieli, A., & Payne, A. J. (2003). Application of control methods for modelling the flow of Pine Island Glacier, West Antarctica. *Annals of Glaciology*, *36*, 197–204.

Virtanen, P., Gommers, R., Oliphant, T. E., Haberland, M., Reddy, T., Cournapeau, D., ... SciPy 1.0 Contributors (2020). SciPy 1.0: Fundamental Algorithms for Scientific Computing in Python. *Nature Methods*, *17*, 261–272. doi: 10.1038/s41592-019-0686-2

Vogel, C. R. (2002). *Computational methods for inverse problems*. Society for Industrial and Applied Mathematics. doi: 10.1137/1.9780898717570

Winberry, J. P., Anandakrishnan, S., Alley, R. B., Wiens, D. A., & Pratt, M. J. (2014). Tidal pacing, skipped slips and the slowdown of Whillans Ice Stream, Antarctica. *Journal of Glaciology*, *60*(222), 795–807.

Wingham, D. J., Siegert, M. J., Shepherd, A., & Muir, A. S. (2006). Rapid discharge connects Antarctic subglacial lakes. *Nature*, *440*(7087), 1033–1036. doi: 10.1038/nature04660

Wright, A., & Siegert, M. (2012). A fourth inventory of Antarctic subglacial lakes. *Antarctic Science*, *24*(6), 659–664. doi: 10.1017/S095410201200048X

Appendix A Velocity Response Functions

The nondimensional horizontal surface velocity perturbations u and v are given by

$$\widehat{u} = -\mathsf{U}_\beta(\nu\widehat{\beta} - \tilde{\tau}\widehat{s}) - ik_x\left(\lambda\mathsf{U}_h\widehat{h} + \mathsf{U}_w\widehat{w}_b\right) \tag{A1}$$

$$\widehat{v} = -\mathsf{V}_\beta(\nu\widehat{\beta} - \tilde{\tau}\widehat{s}) - ik_y\left(\lambda\mathsf{V}_h\widehat{h} + \mathsf{V}_w\widehat{w}_b\right) \tag{A2}$$

where U_f and V_f (f being w_b, β, or h) are response functions (Supporting Information Text S1). The nondimensional velocities (A1) and (A2) have been scaled by the vertical velocity anomaly scale w_0. The response functions for the u component (eq. A1) are given by

$$\mathsf{U}_h = \frac{1}{k^2}\left(2k(\gamma k + 1)(2\gamma + (2\gamma + 1)e^{2k} - 1)e^k + \mathsf{P}_\alpha\right)\mathsf{D}^{-1} \tag{A3}$$

$$\mathsf{U}_w = \left(2\gamma^2 - 3\gamma + 2(2\gamma^2 - 1)e^{2k} + (2\gamma^2 + 3\gamma + 1)e^{4k} + 1\right)\mathsf{D}^{-1} \tag{A4}$$

$$\mathsf{U}_\beta = \frac{k_x^2}{k^3}\Big(2\kappa(\gamma - 1) + k(2\gamma - 1) + 2(2\gamma\kappa + 4\gamma k^2(\kappa - 1) + k(4\kappa - 3))e^{2k} \tag{A5}$$

$$+ (2\kappa(\gamma + 1) - k(2\gamma + 1) - 1)e^{4k} + 1\Big)\mathsf{D}^{-1} \tag{A6}$$

$$\mathsf{D} = \Big((2\gamma^2 + 3\gamma + 1)e^{6k} + (6\gamma^2 + 4\gamma k^2(2\gamma + 1) + 4k(2\gamma + 1) + 3\gamma - 1)e^{4k} \tag{A7}$$

$$+ (6\gamma^2 + 4\gamma k^2(2\gamma - 1) + 4k(2\gamma - 1) - 3\gamma - 1)e^{2k} + 2\gamma^2 - 3\gamma + 1\Big)/(2e^k), \tag{A8}$$

where $\kappa = (k/k_x)^2$ here. The response functions for the v component (eq. A2) are given by

$$\mathsf{V}_h = \mathsf{U}_h|_{\kappa=0} \tag{A9}$$

$$\mathsf{V}_w = \mathsf{U}_w \tag{A10}$$

$$\mathsf{V}_\beta = \frac{k_y}{k_x}\mathsf{U}_\beta|_{\kappa=0}, \tag{A11}$$

setting $\kappa = 0$ here instead. The additional terms P_α entering the expression for U_h (A3) and V_h (A9) when $\alpha > 0$ are given by

$$\begin{aligned}\mathsf{P}_\alpha = c_\alpha\Big(&3\gamma - 2\gamma^2 - 1 + 2\kappa\left(2\gamma^2 - 3\gamma + 1\right) + \Big[2\gamma^2 + 3\gamma - 2\kappa\left(2\gamma^2 + 3\gamma + 1\right) + 1\Big]e^{6k} \\ &+ \Big[-16\gamma^2k^2 - 8\gamma^2k - 2\gamma^2 + 8\gamma k^2 - 12\gamma k - 3\gamma + 2\kappa\big(8\gamma^2k^2 + 2\gamma^2 - 4\gamma k^2 + 8\gamma k \\ &-\gamma - 4k + 1\big) + 8k - 1\Big]e^{2k} + \Big[16\gamma^2k^2 - 8\gamma^2k + 2\gamma^2 + 8\gamma k^2 + 12\gamma k - 3\gamma \\ &-2\kappa\big(8\gamma^2k^2 + 2\gamma^2 + 4\gamma k^2 + 8\gamma k + \gamma + 4k + 1\big) + 8k + 1\Big]e^{4k}\Big).\end{aligned} \tag{A12}$$